Molecular Dynamics Simulation for Size-Dependent Properties and Various Nanoscale Phenomena

Seungho Park[1,#], Joon Sik Lee[2], Young Ki Choi[3], Sung San Cho[1] and Jung Soo Kim[1]

[1] Department of Mechanical and System Engineering, Hongik University, Seoul, Korea
[2] School of Mechanical and Aerospace Engineering, Seoul National University, Seoul, Korea
[3] School of Mechanical Engineering, Chung-Ang University, Seoul, Korea

ABSTRACT

Stimulated by novel phenomena observed in molecular aggregates, recent developments in engineering fields of microscopic scales are creating tremendous opportunities for future nanotechnology-based applications. Investigation in the field involves sub-nanosecond or sub-micrometer interactions between extremely small systems, but researches to date in these physical extremes have been quite limited. Here, we shed light on some of nanoscale phenomena using molecular dynamics simulation: visualization of various phenomena of nanoscales and exploration of size-dependent mechanical properties.

Key Words : Size-dependent properties, Molecular dynamics, Surface tension, Young's modulus

1. Introduction

Computer simulations play an important role in science and engineering as an intermediator between experiments and theories. They serve as powerful tools not only in understanding and interpreting the experiments at the microscopic level, but also in studying regions which are not accessible experimentally, or which would entail very expensive experiments[1].

Among various simulation techniques, molecular dynamics (MD) is one of the most effective tools for studying micro- to nano-scale phenomena since it can yield detailed information on the molecular/atomic motion and structures if appropriate intermolecular potentials are given.

In this paper, emphasis is laid on the simulation of selected evanescent phenomena that can not be observed

readily, or the properties that may vary considerably, as the dimensions are varied at nanoscale.

2. Simulation Model

2.1 The Lennard-Jones Potential

The intermolecular interactions in the MD simulation for estimation of cavitation and surface tensions, and for the visualization of nanojet formation and laser ablation processes are described by the well-known Lennard-Jones (LJ) 12-6 potential,

$$\Phi_{ij} = 4\epsilon\left[\left(\frac{\sigma}{r_{ij}}\right)^{12} - \alpha_{AB}\left(\frac{\sigma}{r_{ij}}\right)^{6}\right], \qquad (1)$$

where r_{ij} is the distance between two molecules, i and j, and ϵ and σ are the representative scales of energy and length, respectively. The parameter α_{ij} controls the miscibility of the solute and solvent molecules[2].

2.2 The Tersoff Three-body Potential

For the simulation of silicon crystallization process and the estimation of Young's moduli, the Tersoff

potential[3,4] is applied under constant-volume and -temperature conditions. In the Tersoff model the potential energy between two neighboring atoms i and j, Φ_{ij} is given by

$$\Phi_{ij} = f_C(r_{ij})[f_R(r_{ij}) + b_{ij}f_A(r_{ij})] \qquad (2)$$

with

$$f_R(r_{ij}) = A_{ij}exp(-\lambda_{ij}r_{ij}) \qquad (3)$$
$$f_A(r_{ij}) = -B_{ij}exp(-\mu_{ij}r_{ij})$$

$$f_C = \begin{cases} 1 & r_{ij} \leq R_{ij} \\ \frac{1}{2} + \frac{1}{2}\cos\left[\frac{\pi(r_{ij}-R_{ij})}{(S_{ij}-R_{ij})}\right] & R_{ij} \leq r_{ij} \leq S_{ij} \\ 0 & r_{ij} \geq S_{ij} \end{cases}$$

where b_{ij} is the multi-body parameter for bond-formation energy affected by local atomic arrangement, especially, by the presence of other neighboring atoms (atom k). Details on the Tersoff potential can be found in references. 3 and 4.

3. Results and Discussion

3.1 Hysteresis and Cavitation[5]

Based on the Lennard-Jones potential in Eq. (1), the cut-off radius r_c beyond which the pair interaction is neglected is set at 4σ without a long-range correction. The time step is $\Delta t = 10 fs$. Some quantities indicated by an asterisk are non-dimensionalized with respect to σ, ϵ, and m, using the values of argon.

For the investigation of cavitation and its hysteretic phenomena, the bubble collapse and nucleation phenomena, which can be observed in the Berthelot tube experiment, are simulated with the LJ molecules contained in a cubic domain of fixed side $L^* = 15.59$ with average density $\rho^*_{avg} = 0.6878$. Fig. 1 describes the variation of the pressure exerted by molecules during the heating and cooling processes. Instantaneous pressures are calculated by the virial representation[6],

$$P = \frac{Nk_BT}{V} - \frac{1}{3V}\sum_i\sum_{i<j}r_{ij} \cdot \nabla\Phi(r_{ij}), \qquad (4)$$

where the first term in the right hand side is for the momentum flux caused by molecular motion and the second term is for that caused by intermolecular forces. After a sufficient equilibration time including period A indicated in Fig. 1, the program enters the production period, which is divided into subperiods B and C. During period B the average temperature of the system is scaled up/down according to the heating/cooling rate of $dT^*/dt^* = 0.016$, while during period C the temperature is maintained at a constant value to relax the system. During the heating process in period B, the pressure increases monotonously with time. Upon entering the relaxation period C it fluctuates around its nearly constant average value. On the contrary, during the cooling process the rate of pressure decreasing is higher than the rate of increasing during the heating process and the pressure is well below its equilibrium value when it enter period C. Even though the temperature is maintained at a constant value during period C, the pressure increases abruptly and approaches the equilibrium value. The hysteresis of the pressure variation during the cycle of heating and cooing processes is dueto the fact that the physical states during the heating process are mainly based on its equilibrium condition, while those during the cooling process enter the metastable condition of high tension, which can be perturbed easily.

Figs. 2 (a)-(f) show a series of the snapshots of the molecule distribution during the heating and cooling processes. In order to observe the existence of vapor bubbles and the nucleation process, the grid of void
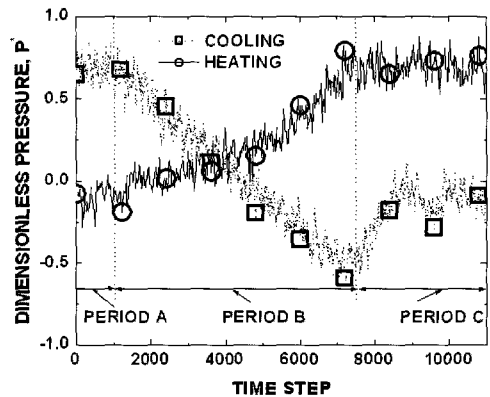

Fig. 1 Pressure variation during heating and cooling processes.

packets is constructed and each void grid is defined as a cubic void, in which there are no molecules within 1.2σ of the void center. In addition, the calculation domain is centerized artificially with respect to the mass center of void packets, which is critical to obtain relevant average shapes of bubbles and their characteristics. In the heating process, the initial temperature in the production period B is 0.694, slightly larger than the triple point of argon. The void distribution is shown in Fig. 2(a), in which a bubble can be observed inside the domain. After 4000 steps, the size of the bubble is reduced due to an increase in the temperature and the pressure increases in the constant volume heating process, as described in Fig. 2(b). After 7500 steps, the temperature is maintained at a constant value. The corresponding snapshot of the void pattern is given in Fig. 2(c), in which stable void packets cannot be observed, since the state of the system has already entered a subcooled liquid state. This distribution can be used as an initial molecular distribution for the cooling process since it can be considered to be an equilibrium distribution of molecules at that state. With this condition the cooling process starts with the same magnitude of the rate of

temperature decreasing as that in the heating process. Fig. 2(d) is the snapshot of the void pattern at 4000 steps and is different from that in the heating process. At this time there is no active nucleation process. At the end of the cooling process (7500 time steps), the void pattern is described in Fig. 2(e), where a stable bubble has not yet been achieved, even though the temperature is the same as that of Fig. 2(a). After some relaxation period, during which the metastable state approaches the stable equilibrium state and the pressure continues to rise as described in Fig. 1, a stable bubble is formed as noted in Fig. 2(f).

One of the interesting parameters obtained from the molecular dynamics simulation, relating to cavitation is the size of microbubbles, whose distribution with respect to the calculation domain size is shown in Fig. 3. The radius shown here is the equimolar dividing radius R_e, which can be obtained from

$$R_e^{*3} = \frac{1}{\rho_g^* - \rho_l^*} \int_0^\infty r^{*3} \frac{d\rho^*}{dr^*} dr^* \qquad (5)$$

At $T^* = 0.818$ the domain size limit for stable bubbles is around 11 and thus the minimum diameter of stable bubbles is about 5.9. For domains smaller than $L^* = 11$, it is difficult to obtain stable bubbles. This could be due to the fact that the critical density for a given domain size approaches that of the spinodal point and thus there exists a strong tendency to nucleate. Once a bubble embryo forms, however, its size is so small

(a) STEP = 1000 (d) STEP = 4000

(b) STEP = 4000 (e) STEP = 7500
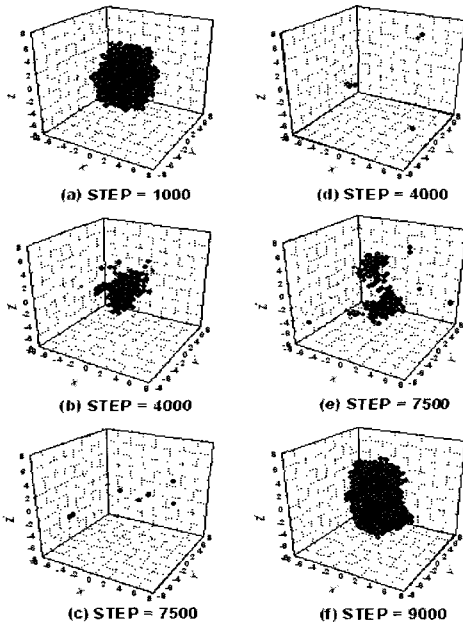
(c) STEP = 7500 (f) STEP = 9000

Fig. 2. Snapshot of void patterns during heating (a)-(c) and cooling (d)-(f) processes.
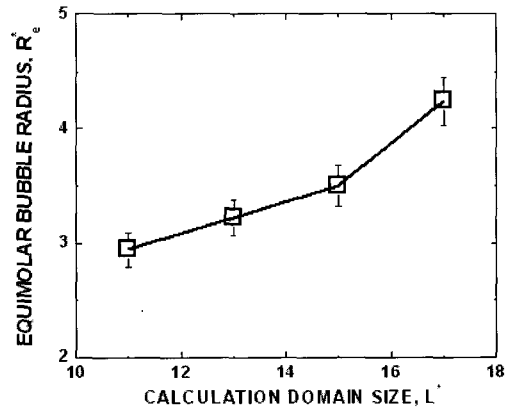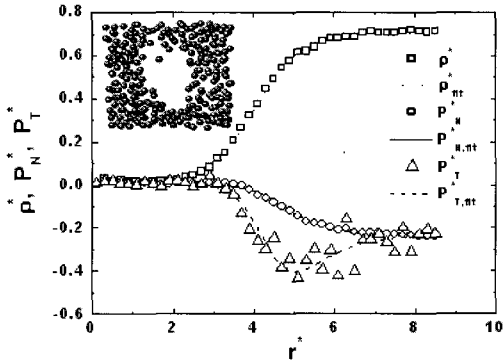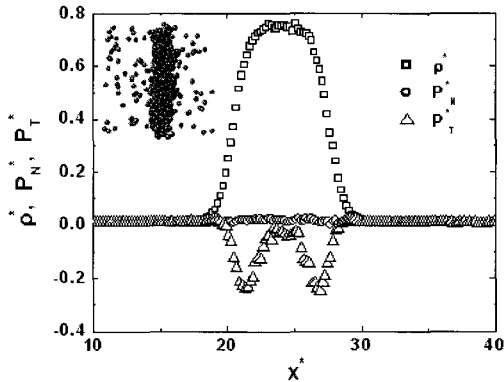

Fig. 3 Equimolar dividing radii of minimum stable bubbles with respect to calculation domain size.
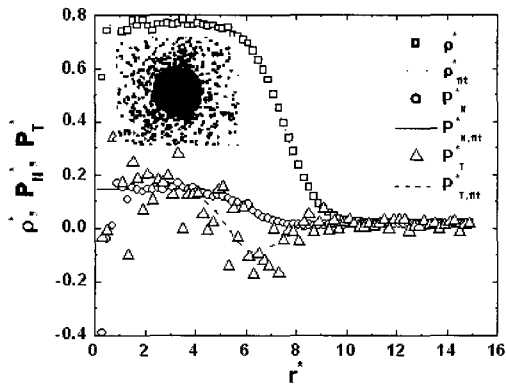
that the liquid-phase is severely stretched and due to the periodic boundary condition the liquid-phase surrounding the bubble embryo is thin enough to break up easily.

(a) Bubbles

(b) Thin films

(c) Droplets

Fig. 4 Profiles of density and pressure tensors.

3.2 Pressure Tensors and Surface Tensions[7,8]

Interfacial phenomena involved in bubbles, thin films and droplets have attracted the attention of researchers for quite a long time due to their wide applications as well as due to their statistical uncertainties in engineering and science field. Fig. 4 describes the density and pressure variations, specifically the normal and tangential components in the interfacial region from vapor- to liquid-phases. The pressure variations differ on each side of the other interfacial region, while the local density increases from vapor-phase to liquid-phase for all cases. For a bubble the normal pressure component decreases from vapor-phase to liquid-phase, for a droplet it increases, and for a thin film it remains constant as that of vapor-phase.

With these pressure tensors surface tensions[6] for each case can be estimated directly using the relation below. For bubbles and droplets

$$\gamma_s^{*3} = -\frac{1}{8}(P_l^* - P_g^*)^2 \int_0^\infty r^{*3} \frac{dP_N^*}{dr^*} dr^* \qquad (6)$$

and for liquid thin films

$$\gamma_\infty = \frac{1}{2} \int_0^\infty (P_N^* - P_T^*) dz^* \qquad (7)$$

Fig. 5 compares the MD estimations of surface tensions with theoretical results for droplets, and bubbles with respect to the equimolar dividing radius. The theoretical model for droplets and bubbles is known as Tolman's model, given by

$$ln\left(\frac{\gamma_s^*}{\gamma_\infty^*}\right) = \int_\infty^{r^*} \frac{\frac{2\delta^*}{r^{*2}}(1 + \frac{\delta^*}{r^*} + \frac{1}{3}\frac{\delta^{*2}}{r^{*2}})}{1 + \frac{2\delta^*}{r^{*2}}(1 + \frac{\delta^*}{r^*} + \frac{1}{3}\frac{\delta^{*2}}{r^{*2}})} dr^* \quad (8)$$

For droplets, surface tensions calculated from the MD simulation agree with the predictions from theoretical estimations. For bubbles, however, surface tensions from the simulations are smaller than those predicted from the theoretical equation and larger than the value of the planar interface within a 15% range, even though there exists a diminishing tendency with

the increase in bubble radii. Here, γ_∞^* is 0.545 in this case, which is obtained from Eq. (7). The reasons for the observed discrepancy are as follows: First, the discrepancy may arise from the periodic boundary conditions used in the MD simulations in contrast to the infinite boundary condition used for the theoretical estimation. Owing to the periodicity of the simulation condition each bubble is exposed to the influence of adjacent bubbles and the liquid-phase between bubbles are confined within the calculation domain. Secondly, as the bubble size decreases, the liquid-phases are severely stretched to satisfy the Laplace equation and the shapes of bubbles are significantly distorted, while theories are based on a spherical shape. Thirdly, the density and pressure distributions are not spherically symmetric, since the liquid-phase region between the adjacent bubbles is not usually thick enough to maintain the spherical uniformity. Lastly, the theoretical model is based on a stationary model, while the bubble shape varies considerably during the production period.

3.3 Heterogeneous Crystallization of Amorphous Silicon[9]

Recently, Ishimaru et al.[10] showed that the *l*-Si and *a*-Si networks generated using the Tersoff potential could reproduce the features of the structural properties obtained by the previous and ab initio calculations. The procedure applied by Ishimaru et al., therefore, is adopted to prepare a realistic amorphous structure of silicon. The main features are: (1) arrangement of atoms in the diamond structure, (2) equilibration of *l*-Si at

Fig. 5 Comparison of surface tensions of bubbles, threads and droplets.

3500 K, (3) quenching and solidification of the *l*-Si to 500 K at a cooling rate of $10^{12} K/s$. They showed that the structural and dynamical properties of *a*-Si generated by a cooling rate of $10^{12} K/s$ were in excellent agreement with those of *a*-Si obtained experimentally, compared with those at other cooling rates. This cooling rate is estimated very close to that achieved in laboratories to prepare *a*-Si by laser annealing. It was reported that the potential energy decreased during the cooling process as shown in Fig. 6 and the kink around 1700-2000 K might correspond to the enthalpy change upon melting of *a*-Si. To understand the kink more clearly, however, variation of structural characteristics such as the number of faces and asphericities are investigated by the Voronoi analysis. Here, the asphericity η is

$$\eta = \frac{S^3}{36\pi V^2} \qquad (9)$$

where S denotes the surface area of the polyhedron and V, its volume. The topological properties obtained from Voronoi analysis are the number of faces, edges, and vertices of the polyhedron and the metric properties are its volume and area. These properties are closely related with the atomic structure of the material under investigation. During the cooling process sudden increases of face numbers and asphericities around 1700-2000 K coincide with the sudden decrease of the potential energy. In addition, the comparison of the potential energy variations during the cooling and heating processes shows that the hysteresis of the potential variations during the cooling and heating cycle is very weak. It implies that the kink is due to the structural changes occurring in solid phase, not due to the abrupt phase-change of the metastable liquid-phase. Here, the number of faces and asphericities are normalized by the values of the diamond lattice of 16 and 2.16, respectively.

For simulating the heterogeneous crystallization process, test specimen with the dimension of $3a \times 3a \times 12a$ including two amorphous-crystalline interfaces is prepared by attaching 12 layers of *c*-Si (216 atoms) as a crystalline seed to a bulk *a*-Si (648 atoms) obtained by the above cooling process and pre-annealed at 500 K for 200 ps. The constant NVT
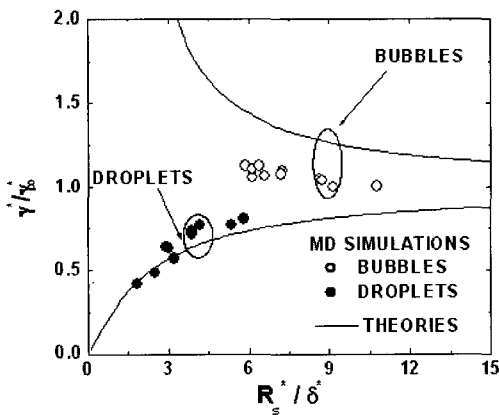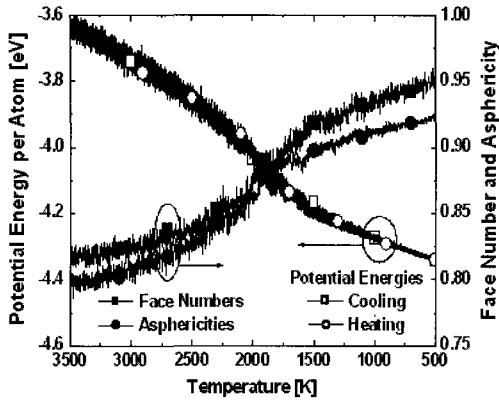
Fig. 6. Potential energies during cooling/heating processes of a-Si and face numbers and asphericities during cooling process with the rate of $10^{12} K/s$.

MD simulations are carried out using the Newton equation and the time step for the integration is set at 2 fs.

Fig. 7 shows the snapshots of the molecular distribution during the external field induced crystallization at 1500 K where five molecules are assumed to be susceptors of external force fields. The initial distribution (time 0 ns) is very similar to that at 500 K. As time goes by, it is shown that the *a/c* interfaces move towards the bulk amorphous region and full crystallization is achieved at around 1.2 ns. Here, open circles denote the *c*-Si seed atoms, while gray spheres denote the atoms originally in the amorphous state. Since melting temperature of Si estimated in the simulation using the Tersoff potential is known to be around 3000 K, the crystallization temperatures in the current simulation range between 1300 and 2200 K. Applying the heating rate of $10^{13} K/s$ from 500 K has attained each temperature of the amorphous/crystalline sample.

3.4 Nanocantilever and Young's Moduli

For the detection of forces in various scanning force microscopy, micro-cantilevers are widely used. Atomic interaction forces, magnetic forces, and electric forces have been monitored using the deflection of the micro-cantilever as a measure of the force. To estimate the forces and inherent thermal noise it is very important to estimate Young's modulus, since the spring constant
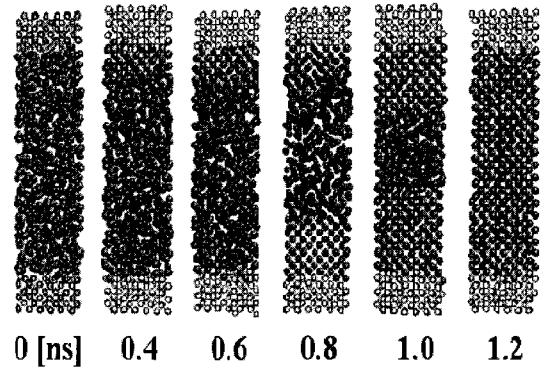

Fig. 7. In [100] direction, snapshots of molecular motion during heterogeneous crystallization at 1500 K under external force fields.

of the rectangular cantilever is modeled as[5].

$$K = \frac{Ewt^3}{4L^3} \qquad (10)$$

where E is Young's modulus and w, t, and L denote the width, thickness, and length of the cantilever, respectively.

For the case of nanoscale cantilever, the thickness of the lever is on the order of nanometers and the surface/interface region may control their static or dynamic behavior. Therefore, it is expected that the mechanical properties will be size-dependent.

Table 1 compares Young's moduli for bulk and thin films of c-Si with respect to the crystalline structure in the longitudinal direction of the lever. As expected, the MD estimations agree well with the values widely applied. As the thickness of the lever decreases, Young's modulus decreases and becomes much smaller than that for bulk Si. The thickness of 1.086 [nm] implies that the film is composed of 8 atomic layers. Atoms in the inner six layers experience the interactions with their neighboring 4 atoms, while atoms on surfaces have interactions with only two neighboring atoms. Therefore, the stiffness decreases in proportion to the contribution of the surface atoms.

3.5 Nanojets and Laser Ablation

One of the important contributions of molecular dynamics techniques is to investigate the phenomena

Table 1 Young's modulus and its size dependency

c-Si	Young's modulus [GPa]					
	bulk			thin film in <100> direction		
direction	<100>	<110>	<111>		1.086	85.85
ref. 11	130.2	168.9	187.5	thickness [mm]	1.629	87.42
MD estimation	130.61	167.79	187.11		2.172	89.95

that is not accessible experimentally, or which would imply very expensive experiments, as well as to understand and interpret the experiments at the micro/nanoscale levels.

Here, the snapshots of the atoms during liquid droplet jetting and laser ablation processes are shown in Figs. 8 and 9. While these phenomena are widely applied in our everyday lives and common electronic fabrication processes, a detailed comprehension of the various underlying mechanisms is still lacking.

Fig. 8 depicts the ablation processes when high energy is imposed on a solid structure. With the snapshot it is easy to observe the melting or desorption of the target. Fig. 9 (a) shows the nanojet ejection failure, when it is assumed that the interactions between the liquid and the nozzle atoms are strong, while Fig. 9 (b) shows a successful liquid droplet ejection when the interactions between the liquid and the nozzle atomsare weak. These affinities can be controlled by the factor α_{AB} included in the Lennard-Jones potential (Eq. (1)).
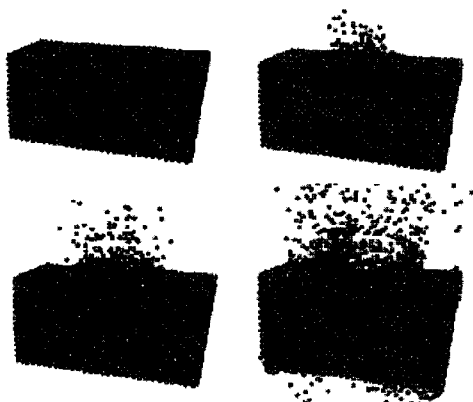

Fig. 8. Simulation for laser ablation.

Fig. 9. Simulation for nanojets with (a) $\alpha_{AB}=1$ and (b) $\alpha_{AB}=0.1$.

4. Conclusions

Using the Lennard-Jones and the Tersoff potentials, MD simulation has been conducted to visualize various microscopic phenomena such as cavitation with negative pressure, nanojet, laser ablation, and crystallization.

To investigate the size-effect on mechanical properties, MD simulation has been applied to estimate surface tensions and Young's moduli. It is shown that surface tensions can vary as the radii of bubbles and droplets vary, which might be due to the interrelationship between the radius of curvature and the number density of the molecules in interfacial regions.

Young's moduli of c-Si have been calculated for various crystalline directions and agree well with the values given in textbooks. It is shown that Young's modulus decreases considerably as the thickness of the structure is reduced and should be taken in account in the design of nanocantilevers.

References

1. Ercolessi, F., A olecular Dynamics Primer, http://www.sissa.it/furio/, pp. 2-3, 1997.

2. Diaz-Herrera, E., Alejandre, J., Ramirez-Santiago, G. and Forstmann, F., "Interfacial Tension Behavior of Binary and Ternary Mixtures of Partially Miscible

Lennard-Jones Fluids: a Molecular Dynamics Simulation, J. Chem. Phys., Vol. 110, pp. 8084-8089, 1999.

3. Tersoff, J., "New Empirical Approach for the Structure and Energy of Covalent Systems," Phys. Rev. B, Vol. 37, No. 12, pp. 6991-7000, 1988.

4. Tersoff, J., "Empirical Interatomic Potential for Silicon with Improved Elastic Properties," Phys. Rev. B, Vol. 38, No. 14, pp. 9902-9905, 1988.

5. Park, S.H., Weng, J.G. and Tien, C.L., "Cavitation and Bubble Nucleation Using Molecular Dynamics Simulation," Microscale Thermophysical Engineering, Vol. 4, pp. 161-175, 2000.

6. Haile, J.M., Molecular Dynamics Simulation, John Wiley & Sons, New York, 1992.

7. Weng, J.G., Park, S.H., Lukes, J.R. and Tien, C.L., "Molecular Dynamics Investigation of Thickness Effect on Liquid Films," J. Chem. Phys., Vol. 113, pp. 5917-5923, 2000.

8. Park, S.H., Weng, J.G. and Tien, C.L., "A Molecular Dynamics Study on Surface Tension of Microbubbles," International Journal of Heat and Mass Transfer, Vol. 44, pp. 1849-1856, 2001.

9. Park, S.H., Kim, H.J., Lee, D.B., Lee, J.S., Choi, Y.K. and Kwon, O.M., "Heterogeneous Crystallization of Amorphous Silicon Expedited by External Force Fields: A Molecular Dynamics Study," Superlattices and Microstructures (to appear)

10. Ishimaru, M., Munetoh, S. and Motooka, T., "Generation of Amorphous Silicon Structures by Rapid Quenching: A Molecular-Dynamics Study," Phys. Rev. B, Vol. 56, pp. 15133-15138, 1997.

11. Tu, K.N., Mayer, J.W. and Feldman, L.C., Electronic Thin Film Science for Electrical Engineers and Material Scientist, Macmillan, 1992.